Deposition of SiC/Si coatings in a microwave plasma-assisted spouted bed reactor

*J.H. van Laar[1,2], H. Bissett[1], J.C. Barry[1], I.J. van der Walt[1] and P.L. Crouse[2]

[1]Applied Chemistry Department, South African Nuclear Energy Corporation SOC Ltd (NECSA), Pelindaba, North West Province, South Africa. *jean@vanlaar.co.za
[2]Fluoro-Materials Group, Department of Chemical Engineering, Faculty of Engineering, Built Environment and Information Technology, University of Pretoria, Pretoria, South Africa.

Abstract: Silicon carbide (SiC) layers were deposited onto alumina particles in a microwave plasma-assisted spouted bed reactor using methyltrichlorosilane (MTS) and hydrogen mixtures, in argon, as precursor gas feed. The operating parameters studied were enthalpy, gas composition, and pressure. Microwaves were guided from a generator, operating at 2.45 GHz, along a rectangular waveguide intersecting a quartz tube, acting as the reaction zone. A graphite nozzle at the bottom of the tube facilitated the spouting action. Growth rates varied from 50 to 140 μm/h. Overall results indicate that the optimal region for SiC deposition requires relatively high enthalpy (~5 MJ/kg) and pressure (>-60 kPa) conditions, with hydrogen-to-MTS ratios ~5:1. The quality (i.e. crystallinity, particle size, Si/C ratios) of the layers improve at these conditions, at the cost of decreased deposition rates. Characterisation was done by XRD, FTIR, XPS, SEM, TEM and EDX, which assisted in developing colour and morphological charts to indicate the changes as a function of changing operating parameters. A microwave plasma spouted bed reactor is demonstrated to be a viable alternative technique for SiC layer deposition onto microspheres.

Keywords: silicon carbide, microwave plasma, spouted bed, methyltrichlorosilane, particle coating

1. Introduction

The high-temperature mechanical performance of silicon carbide (SiC) is an important factor contributing towards its use as a fission product barrier in tri-isotropic (TRISO) fuel, and its consideration as a host material for high level radioactive waste immobilisation [1]. As a nuclear ceramic, SiC exhibits excellent mechanical properties and dimensional stability under irradiation and is a proposed replacement material for zirconium alloy-based fuel cladding in light water reactors [2]. Next generation high-temperature reactor (HTR) designs currently project operating temperatures up to 1000 ℃ which emphasises the importance of a thorough understanding of the SiC layer properties and deposition mechanisms [3]. The current standard method for TRISO fuel fabrication involves chemical vapour deposition (CVD) in a fluidized bed furnace [4]. This technique, although stable and reliable, demands a high-energy input to provide the necessary temperatures needed for the decomposition of methyltrichlorosilane (MTS) to form SiC. The synthesis reaction is shown in Eq. (1), and is thoroughly reported in the literature [5-7]

$$CH_3SiCl_3(l) \rightarrow SiC(s) + 3HCl(g) \tag{1}$$

Various plasma-enhanced chemical vapour deposition (PECVD) techniques have been investigated for the synthesis and deposition of SiC [5, 8, 9]. Among these techniques, microwave plasma-enhanced CVD (MW-PECVD) has produced promising results [10-14], and provides economic advantages such as decreased energy requirements and reduced equipment footprints [15]. In combination with this plasma technique, fluidised -and spouted bed reactors have also produced promising results for deposited coatings on particles [16, 17] due to the added advantage of high mass- and heat-transfer rates, and high bulk temperatures [18].

In this study, a microwave plasma-assisted spouted bed reactor was used for the *in situ* synthesis and deposition of SiC layers onto alumina spheres in order to investigate MW-PECVD as a viable alternative deposition process for high quality

SiC layers. MTS was used as precursor, and argon served as both plasma and carrier gas. The effect of hydrogen-to-MTS molar ratio (H_2:MTS) was investigated, as well as the effect of reactor pressure and enthalpy on the deposited layer characteristics.

2. Experimental

2.1 Plasma-assisted Deposition Apparatus

The experimental setup consisted of a commercial microwave source from Electronic GmbH & Co. (model no. PGEN2450/1.5–1.5KW2AIW) as presented in Figure 1. The equipment included a 1500 W power supply with MOS-FET amplifier, a microwave generator operating at 2.45 GHz and a water-cooled magnetron. The microwaves were guided from the generator along a rectangular waveguide fitted with three stub tuners and a sliding short. A quartz tube, with inside diameter 20 mm and length 300 mm, was mounted between two support flanges, and positioned perpendicular to the metallic waveguide between the stub tuner and the sliding short. The support flanges also served as in- and outlets to allow flow through the plasma zone. A graphite nozzle was inserted into the bottom of the quartz tube to bring about the spouting action of the bed. The nozzle was designed with a conical angle of 45º and an inlet diameter of 1.5 mm. A metallic grid was inserted into the top flange to prevent particles exiting the reaction zone.
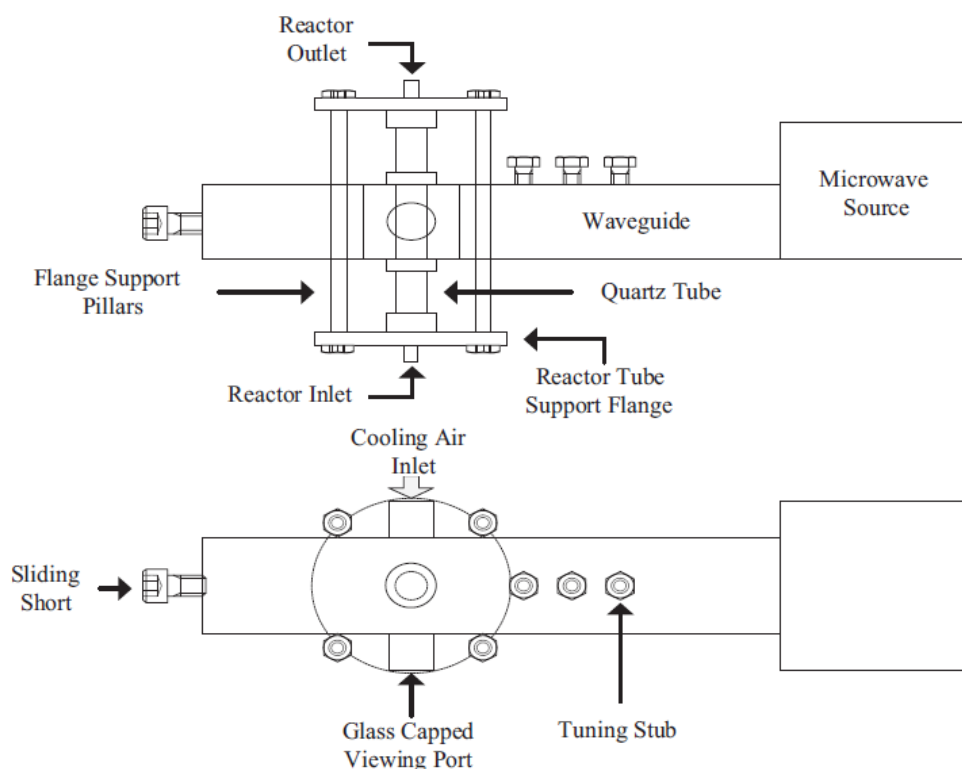

Figure 1: Physical layout of reactor assembly.

Argon and hydrogen flow rates were regulated using Aalborg rotameters. MTS was fed into the reactor through the sweeping action of an additional argon stream diverted through the MTS container. The MTS vaporisation assembly consisted of a 250 mL borosilicate glass jar equipped with a lid containing an inlet and outlet port. The argon inlet line was placed above the liquid MTS level, enabling diffusion of MTS into the argon stream. The rate of MTS mass diffusion into the argon stream was calibrated through a series of runs, at various argon flow rates. After passing through the reaction zone, the exiting gas stream was fed through a $Ca(OH)_2$ scrubber to remove HCl and any unreacted MTS from the waste stream before entering an extraction system. A valve at the reactor exit allowed for easy control of the reactor pressure during operation. The schematic representation of the complete experimental flow path is shown in Figure 2.
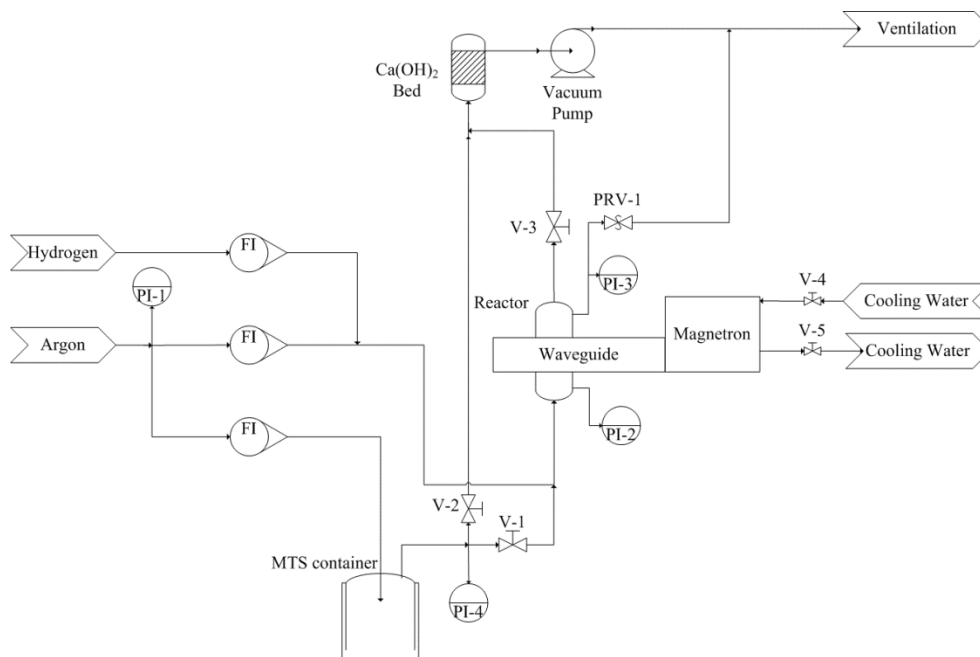
Figure 2: Schematic representation of the flow path of the experimental assembly.

2.2 Materials

MTS served as precursor material (>99.0 % a/a) obtained from Merck & Co. Inc. Argon and hydrogen gas cylinders were obtained from African Oxygen Limited (Afrox) with >99.9% purity. The alumina spheres (Microbit Leonardo Microbeads) had a size distribution of ⌀ = 1.5 to 2.5 mm, and a total bed mass of approximately 1 g (50 spheres) was used per experimental run.

2.3 Experimental Design for Deposition Experiments

The argon plasma was initiated under vacuum (-85 kPa gauge pressure), using an Alcatel 2010I duel-stage rotary vane pump. The argon flow was gradually increased to exceed the spouting velocity. Hydrogen was then fed into the reactor, and the pressure gradually increased. After the desired pressure and hydrogen flow rates were reached, the MTS was fed into the system. During experimental runs, the alumina spheres darkened in colour, and a black/brown powder deposited on the inner wall of the quartz tube. The spheres were collected after runs, and the powder was flushed from the tube walls using acetone. The acetone was evaporated in a fume hood, and the powders were collected.

The experimental parameters are shown in Table 1. The design of experiments (DoE) was of a Box-Wilson 3-dimensional central composite design (CCD), covering a wide range of experimental parameters, within the capability of the system. This CCD comprises of an imbedded factorial design with a centre point that is surrounded by a group of 'star points' to allow for estimation of the curvature shown in Figure 3. These star points are at a fixed distance $\alpha = [2k]^{\frac{1}{4}}$, where k is the number of factors [19].

3

Table 1: Experimental Parameters.

Exp. No.	Spout velocity (L/min)	MTS flow (g/h)	H$_2$:MTS (mol:mol)	Power (W)	Pressure (kPag)
1	6.35	7.32	2	700	-50
2	6.35	7.32	8	700	-70
3	6.35	7.32	5	1000	-60
4	6.35	7.32	5	1000	-80
5	6.35	7.32	5	1000	-60
6	6.35	7.32	5	1000	-40
7	6.35	7.32	5	1000	-60
8	6.35	7.32	5	500	-60
9	6.35	7.32	8	700	-50
10	6.35	7.32	2	1290	-70
11	6.35	7.32	8	1290	-50
12	6.35	7.32	2	700	-70
13	6.35	7.32	8	1290	-70
14	6.35	7.32	10	1000	-60
15	6.35	7.32	5	1500	-60
16	6.35	7.32	0	1000	-60
17	6.35	7.32	2	1290	-50

2.4 Instrumentation for Characterisation

High-resolution scanning electron microscopy (SEM) was performed on the particles using a Zeiss Ultra Plus Field Emission Scanning Electron microscopes (Carl Zeiss, Germany) and transmission electron microscopy (TEM) was performed using a Phillips 301 instrument. Elemental mapping and energy-dispersive X-ray spectroscopy (EDX) were performed using a Quanta 200 3D SEM with an Apollo X Silicon Drift Detector (SDD). Powder X-ray diffraction (XRD) was conducted with a PANalytical X'pert Pro diffractometer using Co K$_\alpha$ radiation. The peak assignments were made using the databases supplied from the instrument manufacturer. X-ray photoelectron spectroscopy (XPS) was conducted using a Thermo ESCAlab 250Xi instrument, and verified with the PHI 5000 Scanning ESCA Microprobe. The peak deconvolutions were applied with assistance from the operators using the data reduction software package PHI MultiPak v9, using Gaussian-Lorentz fits. Optical photography was undertaken using a Nikon D7000 camera with AF-S Nikkor 18-200mm lens. Fourier Transform Infrared Spectroscopy (FTIR) was performed using a Bruker T27 Tensor spectrometer.

3. Results

3.1 Deposition Rates and Kinetics

The system enthalpy, H_{TOT}, which applies to all the gaseous components present in the system (argon, hydrogen and MTS), was calculated using Eq. (1)

$$H_{TOT} = \frac{P_f - P_r}{\dot{M}_{TOT}} \tag{1}$$

where P_f is the forward power, P_r is the reflected power, and $\dot{M}_{TOT}$ is the total mass flow rate. The resulting deposition rates and growth rates are presented in Table 2. Deposition rates were determined by the mass differences of the particles before and after runs. The growth rates were calculated by measuring the layer thicknesses on calibrated SEM micrographs. Using two independent methods has the added benefit of reducing possible measurement errors. The results appear to be in relative agreement with higher mass deposition rates tending to show higher layer growth rates. It should be noted, however, that embedding the particles in the organic resin often damages the SiC layer, making accurate layer thickness measurements difficult. Depending on the operating conditions, the growth rates varied from 50 to 140 μm/h.

The effects of the varying parameters on these results are represented using 3D surface contour plots, shown in Figure 3. These plots were generated using quadratic polynomials in the form of Eq. (2)

$$y = c_o + c_1 X_1 + c_2 X_2 + c_3 X_3 + c_4 X_1 X_2 + c_5 X_1 X_3 + c_6 X_2 X_3 + c_7 X_1^2 + c_8 X_2^2 + c_9 X_3^2 + \cdots \qquad (2)$$

where X_1 represents enthalpy, X_2 represents H$_2$:MTS molar ratio, and X_3 represents system pressure. The values for the coefficients are given in Table 3 for the mass deposition and layer growth rates, respectively. An additional term, also shown in Table 3, was added to each polynomial to improve overall fit with minimal effect on the overall shape of the curves.

Table 2: Results of deposition -and growth rate measurements.

Exp. No.	Deposition Rate (g/h)	Layer Thickness (μm)	Run Time (s)	Growth Rate (μm/h)
1	0.035	18.2	1304	50.2
2	0.060	17.1	1208	51.0
3	0.090	26.9	1200	80.7
4	0.208	47.2	1198	141.7
5	0.078	32.2	1216	95.3
6	0.116	24.3	1204	72.6
7	0.119	36.4	1200	109.3
8	0.030	17.5	1199	52.5
9	0.029	24.7	1200	74.2
10	0.180	36.0	1200	108.1
11	0.060	25.1	1200	75.2
12	0.060	26.2	1200	78.5
13	0.012	23.9	1199	71.6
14	0.067	23.9	806	106.7
15	0.090	22.5	1198	67.5
16	0.030	29.5	1201	88.5
17	0.077	24.7	1200	74.0

Table 3: Values for polynomial coefficients.

Response	c_o	c_1	c_2	c_3	c_4	c_5	c_6	c_7	c_8	c_9	Add. Term	C_{10}
Mass Dep.	0.459	2.34E-3	-0.037	0.021	0.023	-2.52E-3	-1.39E-3	-0.013	-2.46E-3	1.33E-4	$C_{10} X_1 X_2 X_3$	5.04E-4
Growth Rate	645.7	-380.1	25.88	13.50	-1.162	-8.089	0.318	50.02	-0.270	8.86E-3	$C_{10} X_1^2 X_3$	1.038

The statistical relevance of these results was verified by an Analysis of Variance (ANOVA), which is summarised in Table 4 for both models.

Table 4: Summary of the ANOVA results for each deposition model.

Response	Model F –value	Model p-value	Lack of fit p-value	Most significant term	Least significant term	R-squared	Pred. R-squared	Adeq. Precision
Mass Dep.	3.07	0.091	0.228	Pressure	H_2:MTS	0.836	-0.926	5.97
Growth Rate	2.90	0.102	0.450	Pressure	H_2:MTS	0.829	-1.84	7.22

In both cases, the model F-values are approach 3, implying there is an approximate 10 % chance that F-values this large could occur due to noise. Additionally, the lack of fit p-values > 0.05 indicate that there is a non-significant lack of fit, which is a requirement for an adequate model. The adequate precision furthermore measures the signal to noise ratio. A ratio greater than 4 is desirable. The reported ratios of 5.97 and 7.22 indicate adequate signals. In both cases, the models can therefore be used to navigate the design space; however, caution is always advised when doing so.

Both models indicate the most significant term to be pressure, which is apparent from the surface contour plots in Figure 3. The least significant terms are those for the H_2:MTS molar ratios.
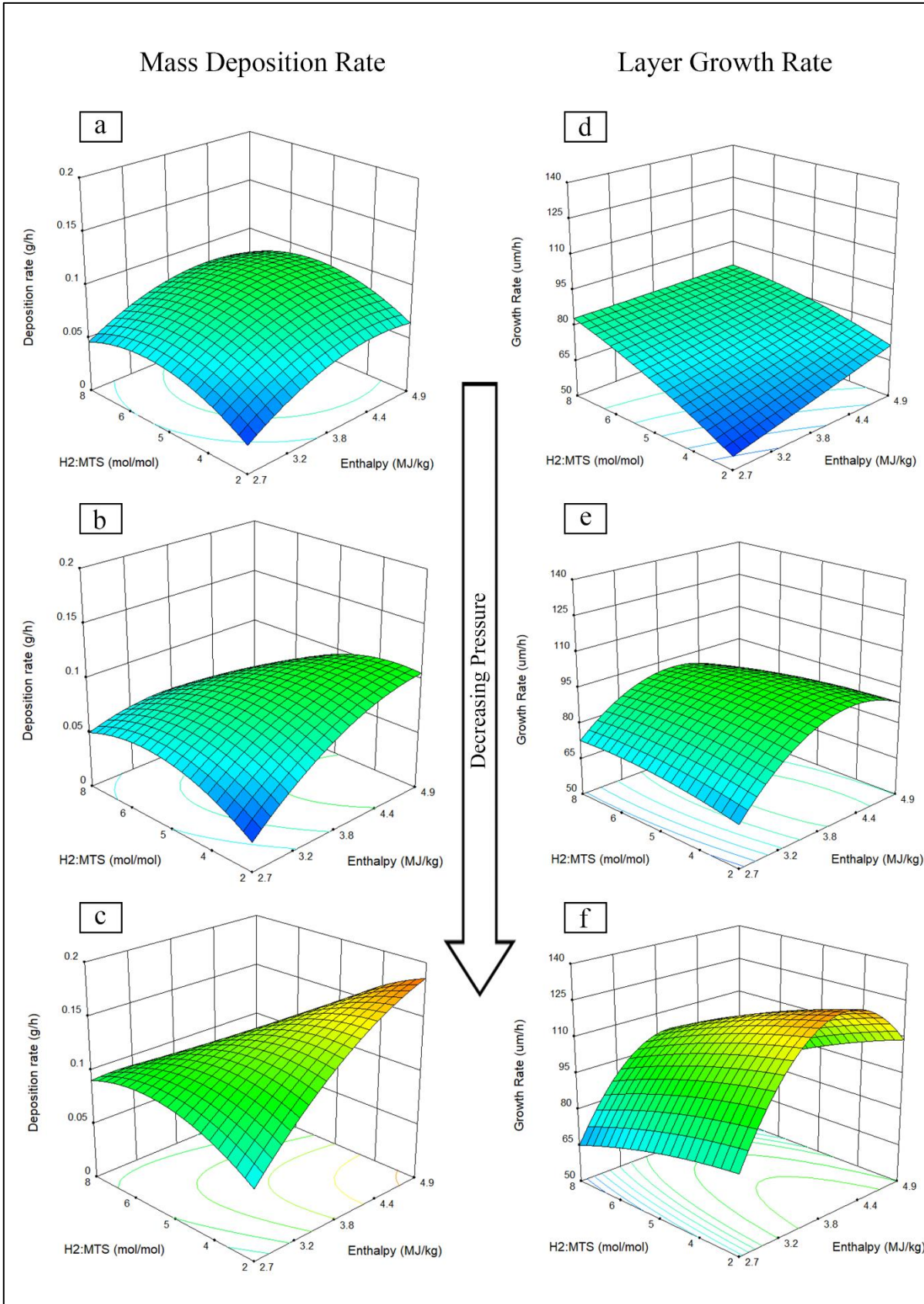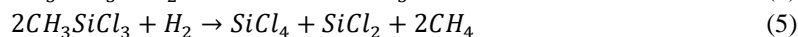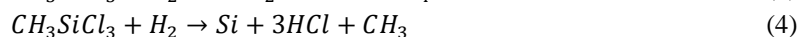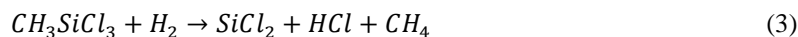
Figure 3: Surface contour plots depicting the effect of varying operating parameters on the mass deposition rate (a - c) and the layer growth rate (d - f).

When considering the surface contour plots representing the mass deposition and layer growth rates (Figure 3), it is evident that an increase in enthalpy generally increases the deposition rate. This follows the expected Arrhenius type dependence on temperature of Eq. (1) with a broad range of activation energies summarised in [5]. In this study, increasing the microwave power (enthalpy) increased the plasma temperature resulting in increased deposition rates. Likewise, an increase in H_2:MTS ratio generally resulted in an increase in deposition rate. Hydrogen not only provides a more reducing environment, but likely takes part in the homogeneous decomposition reactions of MTS at low temperatures leading to solid deposition (SiC, Si or C) [5], given by Eqns (3), (4) and (5) [20].

$$CH_3SiCl_3 + H_2 \rightarrow SiCl_2 + HCl + CH_4 \qquad (3)$$
$$CH_3SiCl_3 + H_2 \rightarrow Si + 3HCl + CH_3 \qquad (4)$$
$$2CH_3SiCl_3 + H_2 \rightarrow SiCl_4 + SiCl_2 + 2CH_4 \qquad (5)$$

From these reactions, SiC is deposited through Eqns (6) and (7).

$$CH_4 + Si \rightarrow SiC + 2H_2 \qquad (6)$$
$$SiCl_4 + CH_4 \rightarrow SiC + 4HCl \qquad (7)$$

When H_2:MTS ratios are very high though, the deposition rate is negatively influenced at low pressure settings. This is possibly related to the high energy demand of hydrogen dissociation and ionization [21]. At lower pressures, the mean free path of the particles is much larger, and collisions are less frequent. The plasma is consequently further from thermal conditions, resulting in lower temperatures, and possibly biased chemical reactions. Increasing the hydrogen concentration requires additional energy input, which affects the plasma enthalpy and consequently temperatures and reaction rates.

Pressure, however, appeared to have an opposite effect, increasing the deposition rate as it decreases. This effect seems to persist for most settings of enthalpy and H_2:MTS ratios, although it appears to be much more prominent at high enthalpies. This trend is likely explained by the decrease in particle collisions associated with decreased operating pressures. Subsequently, non-thermal plasma conditions arise with operating temperatures below 1 300 K, which favours the production of silicon-rich deposits [5, 15, 22, 23]. It is possible that at these conditions, the deposition of Si is favoured, resulting in an apparent increase in the deposition rate. With regards to this experimental system, however, decreasing the operating pressure also affects the pressure inside the MTS container. This allows for a slight increase in MTS concentration in the feed stream, resulting in increased particle growth rates [24, 25]. It is also possible that decreasing the operating pressure will exacerbate any potential atmospheric leaks in the system, and increase the amount of SiO_2 formed during runs. The quality/composition of the layers may therefore provide a more accurate explanation of the observed trends.

The kinetics of the deposition mechanism were further investigated by repeating an experiment for varying run times, while keeping the operating parameters constant. Seven runs were completed, varying from 3 to 40 minutes, and for each run a new batch of alumina spheres was used. The experimental parameters were set to that of experimental point no. 3 (the central point). The results are shown graphically in Figure 4, which indicated that two regimes are present with regards to the gradient of the deposition rate. This is in contrast to the expected outcome of a single deposition rate gradient. A possible explanation entails a change in plasma enthalpy during each run, brought about by the additional deposition of SiC on the quartz tube. This layer of SiC could potentially hinder the penetration of microwaves into the plasma [26, 27], an effect which is worsened with time and appears to stabilise after approximately 10 minutes. Additionally, the powders collected from the quartz tubes after each of these runs, were submitted for XRD analysis. The XRD patterns are shown in Figure 5, and indicate an increase in the ratio of crystalline to amorphous material with increasing run time. The unlabelled peaks are those of silicon.
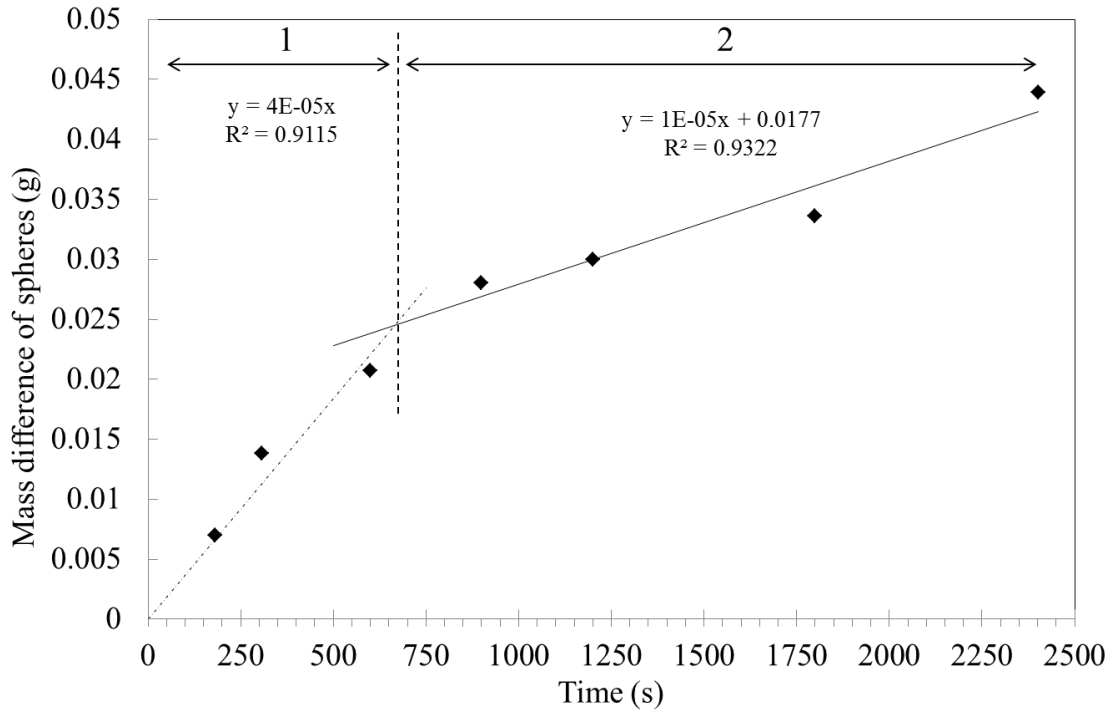
8

Figure 4: Kinetics of the SiC deposition mechanism.

The relative phase amounts of crystalline material (weight %) were estimated using the Rietveld method with the software program X'Pert Highscore Plus, and are given in Table 5.

Table 5: Relative phase amounts (weight %) from XRD patterns.

Time (min)	5	10	15	20	30	40
Si %	27.3	23.3	20.0	19.2	18.1	28.8
SiC %	72.7	76.7	58.0	80.8	81.9	71.2
Quartz %	-	-	22.0	-	-	-
SiC/Si	2.66	3.29	2.90	4.20	4.52	2.47

The relative phase amounts reported are those of the crystalline material only. The ratio of silicon carbide to silicon (SiC/Si) ranges from 2.47 to 4.52, while a run time of 30 minutes yielded the highest SiC/Si ratio of 4.52. A high percentage of crystalline SiO_2 (quartz) was identified in the sample running for 15 minutes. This anomaly is likely due to contamination from the quartz tube during collection of the powders.

9
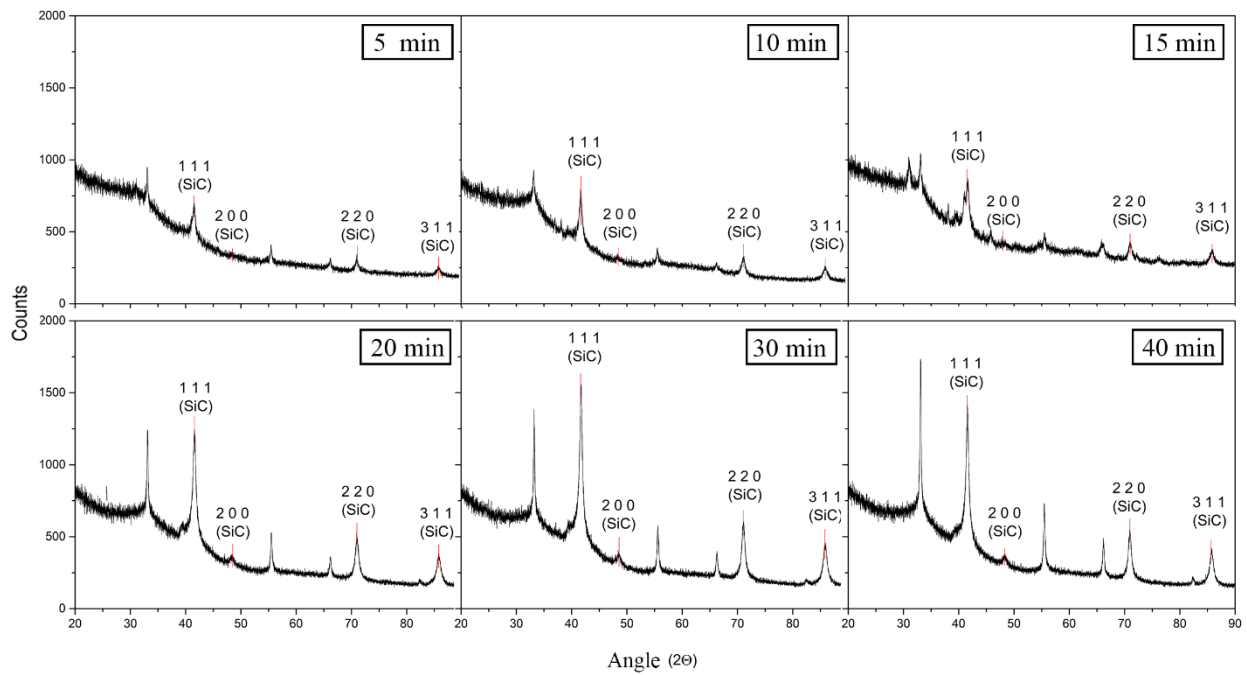
Figure 5: Graphical depiction of the change in XRD spectrum with run time.

3.2 Morphology and Elemental Mapping

The deposited layers were characterised using scanning electron microscopy (SEM) and energy-dispersive X-ray spectroscopy (EDX). The surface morphologies vary in structure. Micrographs of two different samples are shown in Figure 6. The two samples shown are: Exp #3 (left) and Exp #4 (right). Both are shown at $10^3 \times$ magnification (*a* and *b*) and $10^5 \times$ magnification (*c* and *d*), respectively.
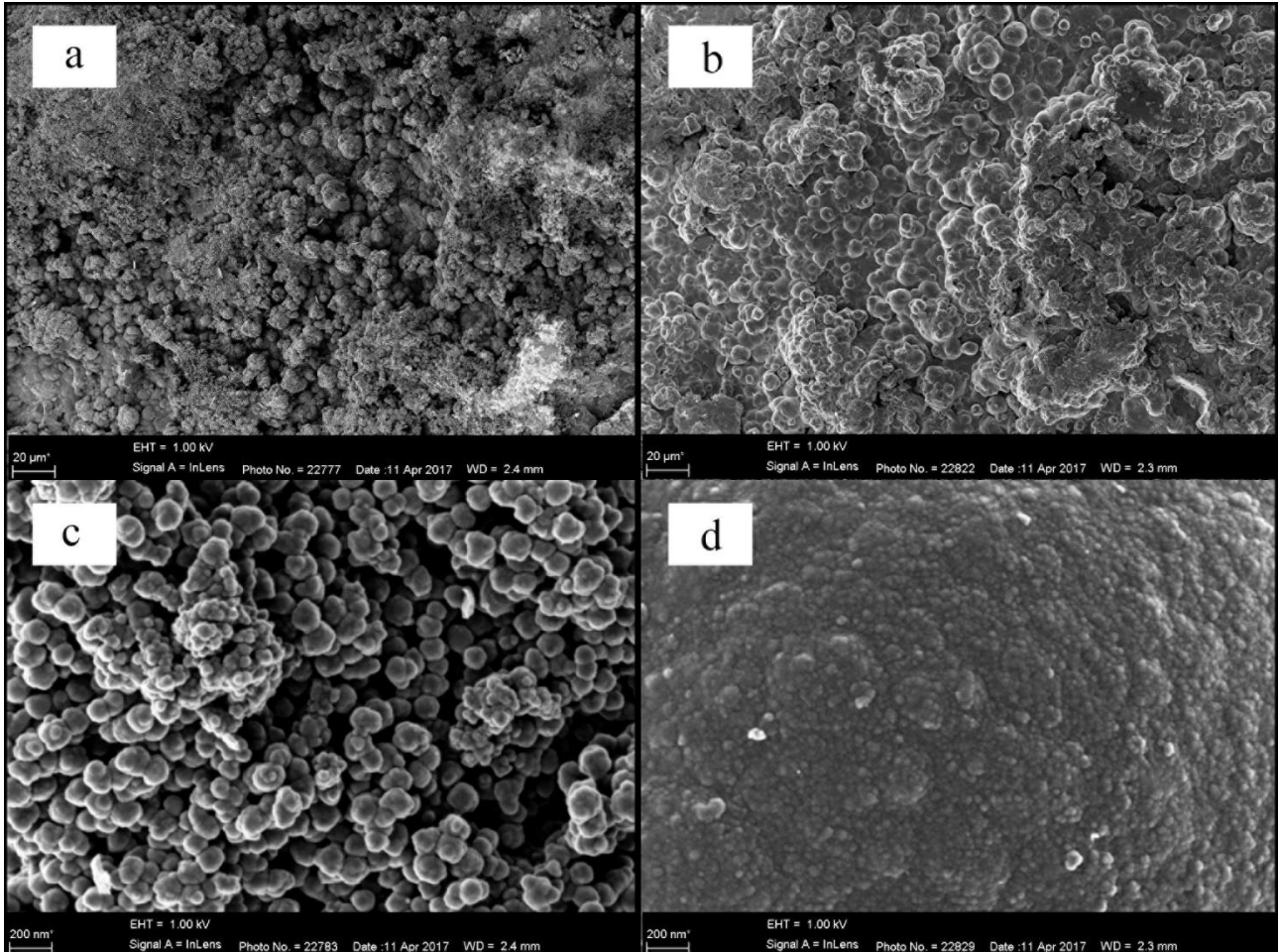
Figure 6: SEM micrographs illustrating the varying morphologies and apparent particles sizes between sample 3 (a and c) and sample 4 (b and d).

At $10^3 \times$ magnification, the morphologies likewise appear to consist of quasi-spherical agglomerates; however, the light (electron) scattering appears different (possibly due to positioning, height, contrast settings etc.). At $10^5 \times$ magnification, however, these agglomerates appear very dissimilar. The quasi-spherical structures are still present in Exp #3, however the agglomerates in Exp #4 appear to consist of much smaller particles, densely packed together. This difference in nanoscale morphologies could potentially result in different macroscopic properties of the layers.

The particles were then embedded in an organic resin, followed by grinding and polishing of the surface until the cross sections of the particles were clearly visible. SEM micrographs of these cross sections were then used for layer thickness measurements, as well as elemental mapping using EDX. Experiment numbers 3 and 4 are again shown as examples in Figure 7.
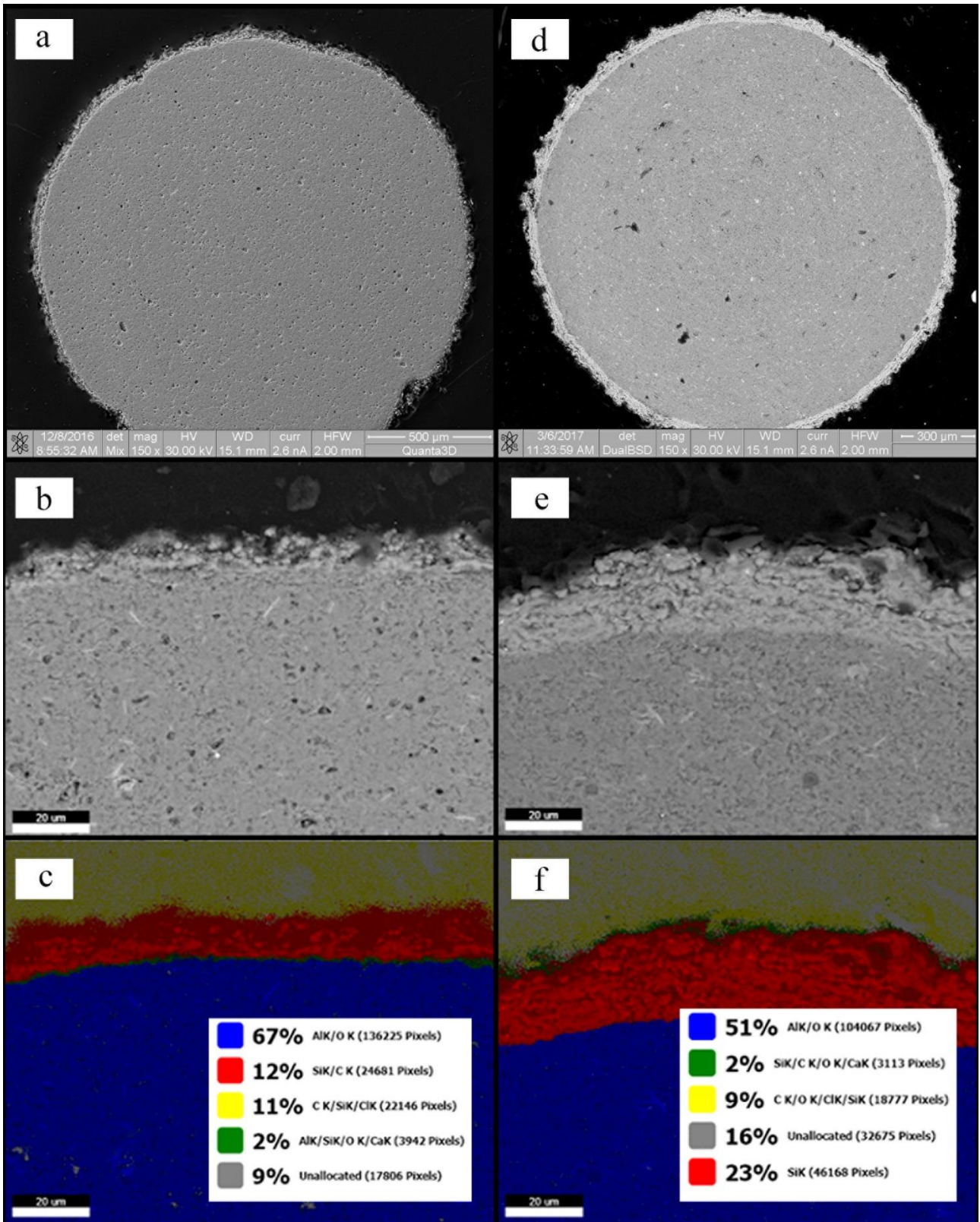
Figure 7: SEM micrographs of the particle cross sections (a and d) and elemental mapping (c and f) indicating the presence of deposited layers on the surface and their different compositions.

During elemental mapping, three distinct phases were identified based on the relative elemental compositions. EDX indicated a silicon/carbon phase in Exp #3 (marked as red), however this phase is not similarly identified for Exp #4. It is instead identified as a silicon rich layer (also red). These values should be considered with caution though, as it is well known that the identification of carbon is somewhat unreliable using EDX techniques. These images are presented here to serve as a proof of layer deposition, rather than an investigation into the composition of the layer.

3.3 Optical Characterisation

A change was also noted in the colour of the final particles between experimental runs, illustrated in Figure 8, similar to the morphological changes accompanying the varying operating parameters,

Figure 8: Photographs demonstrating the difference in colour of the final particles from experiments 4 (a), 6 (b) and 10 (c).

Further investigation suggested that these colours are strongly influenced by the pressure and enthalpy conditions, whereas hydrogen concentration has a negligible effect. It is expected that the appearance of these colours are the direct result of the underlying morphological, and possible crystalline structures, inherent in the deposited layers, as well as their elemental composition. A generalised "colour chart" was accordingly created, shown in Figure 9, which uses the Pantone® colour matching system. The interpretation of colour differs between observers, computer monitors and printers, and therefore it is convenient to use a standard catalogue for user reference. The corresponding Pantone® colour identified for each region in Figure 9 is reported in Table 6. Determining the colours involved importing the images to Adobe Photoshop CC 2017, sampling numerous pixel colours, and ultimately extracting an "average" colour from the built-in Pantone® catalogues.

Table 6: Pantone® references for each corresponding region shown in the colour chart.

Region	I	II	III	IV	V	VI	VII	VIII	IX
Pantone Reference	7532 C	7554 C	7554 C	462 C	Black 4C	431 C	440 C	Neutral Black C	Black C

Accordingly, the same chart template was used to visually represent the changing morphologies within the same regions, shown in Figure 10 using SEM micrographs. The transitions between the regions are not sharp, but rather indicate a gradual change in colour and morphology as the process parameters are varied.
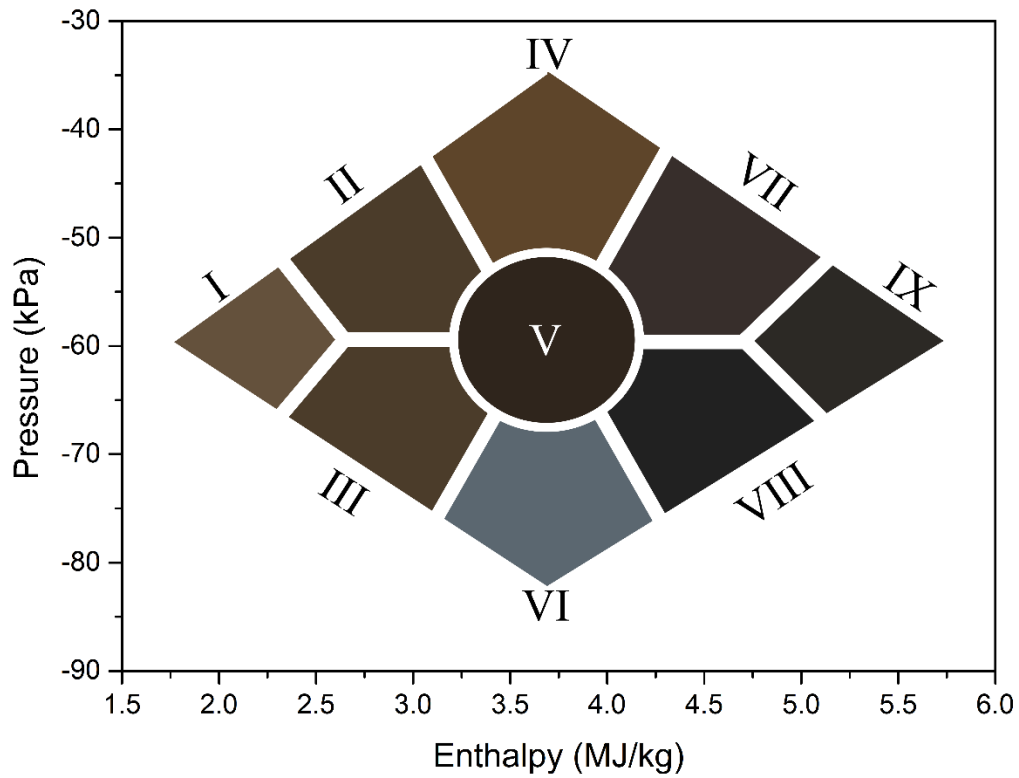
Figure 9: Colour chart representing the various particle colours within the design space.
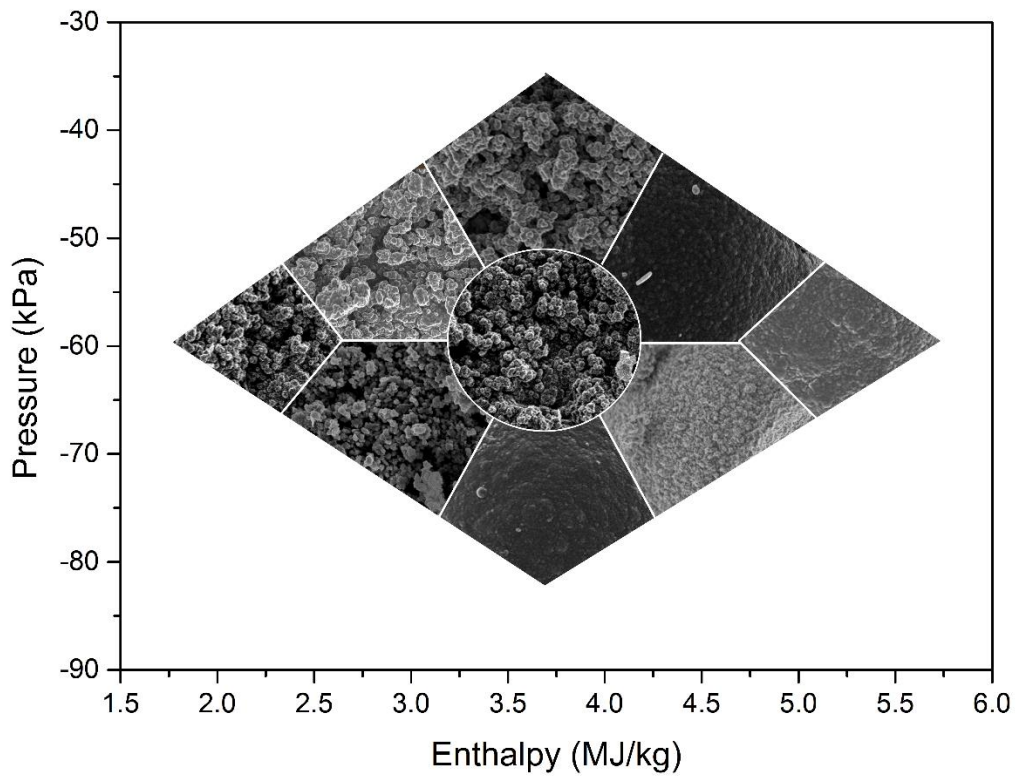

Figure 10: Similar chart showing the various morphologies throughout the design space.

The resulting graph indicates that higher enthalpy values and lower pressures generally result in darker colours accompanied by smaller particle sizes (regions VI to IX), whereas lower enthalpy values and higher pressures result in slightly lighter colour variations accompanied by larger quasi-spherical agglomerates (regions I – V). The colour variations are likely brought about by varying elemental compositions and/or microscopic variations in the accompanying morphological map. The changes in morphology are explained by the effect of the operating conditions on particle size. The temperature of a plasma system is strongly influenced by the microwave power, and a strong link is apparent between microwave power and particle size [25, 28]. When microwave power is increased, the particle size decreases, which is evident in the different morphologies presented in Figure 10. This result is supported by theoretical calculations done by Vennekamp *et al.* [14]. At lower power, the reactivity of the plasma results in a smaller number of nuclei. Molecules formed by the chemical reaction condense in the few nuclei, resulting in larger particles. Likewise, at higher power, more nuclei are formed, and thus smaller particle sizes are obtained [29]. Pressure, however, has an opposite effect, and appears to increase the particle sizes as it increases. This correlation is justified when compared to the literature [28, 30], as an increased pressure would allow for increased particle collision probability, resulting in enhanced particle growth.

3.4 SiC identification through X-ray Diffraction and FTIR Spectroscopy

Powders collected from the quartz tubes were submitted for XRD analysis. The presence of β-SiC (cubic) was confirmed for most samples, as well as the presence of silicon. The occurrence of broadened peaks suggests the presence of amorphous SiC, and its relative proportion varies between experimental runs. It was also uncertain whether the powders collected from the quartz tubes were identical in composition to that of the layers deposited on the particles. XRD and FTIR spectroscopy were subsequently used to confirm this assumption by comparing the powdered samples' spectra directly with those of the deposited layers. To this end, particles from the central point were sonicated in ethanol, where after the ethanol was evaporated and the particles removed. The remaining powders were collected and submitted for XRD and FTIR analyses. The spectra are compared directly to those of the powders collected from the quartz tube during the same run. The XRD comparison is shown in Figure 11. The comparatively small peaks of the sonicated powders are likely due to the small amount of powder available for the analysis, which approaches that of the lower detection limit of the instrument.
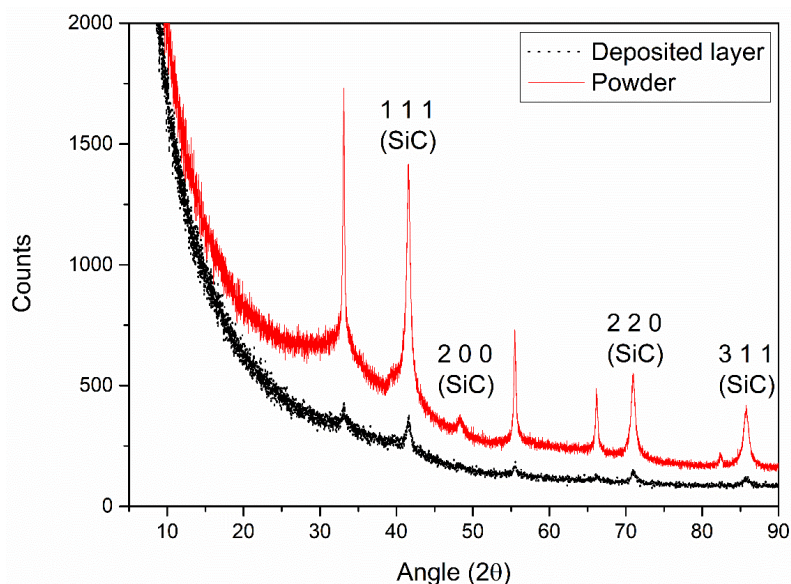

Figure 11: XRD-based comparison of the powders collected from the quartz tubes with those of the deposited layers on the particles.

Relative phase quantification using the Rietveld method, indicated that the powder and sonicated samples had similar SiC/Si ratios of 2.47 and 2.79, respectively. The FTIR comparison is shown in Figure 12. A standard β-SiC sample,

obtained from Sigma-Aldrich, is also compared here as an additional verification of the presence of SiC in the product samples. The corresponding positions of the troughs are indicative of β-SiC, despite the large difference in the y-axis scales. Positions A and B are located at approximately 770 cm^{-1} and 1060 cm^{-1}, corresponding to bonded Si-C stretching and S-CH$_2$ rocking or wagging [20, 31]. Position B could alternatively be associated with Si-O stretching [20, 32].
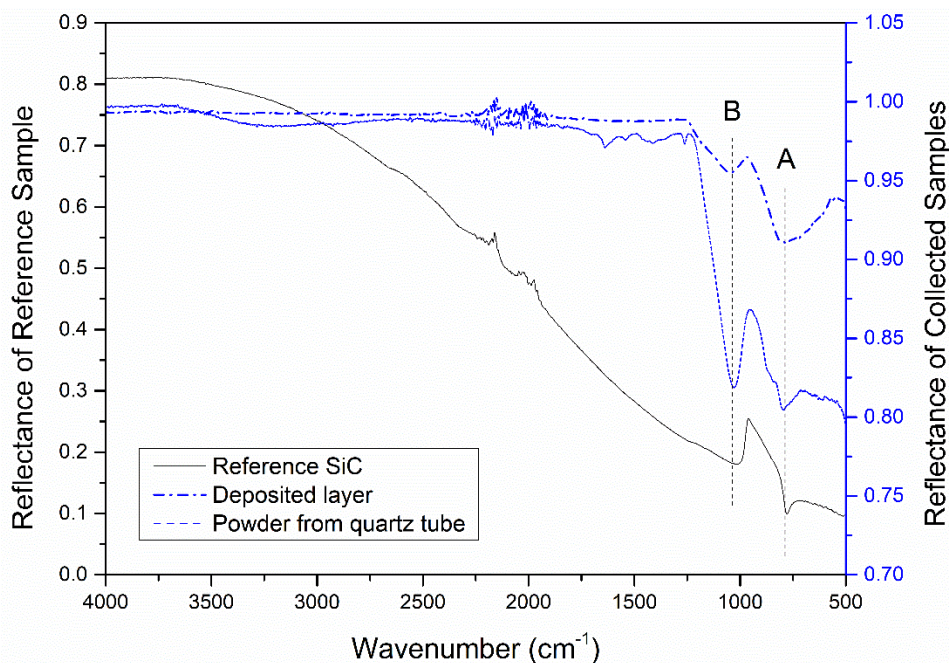

Figure 12: FTIR spectrum of the collected powders compared to a β-SiC reference sample.

Additionally, the powders were collected from the runs corresponding to the lower and higher pressure and enthalpy limits, namely experiment numbers 4, 6, 8 and 15. These powders were submitted for XRD analysis and the results are shown in Figure 13. The corresponding phase amounts of crystalline material (weight %) were estimated and are reported in Table 7. The high amount of amorphous material means that these results might be less reliable than those reported earlier in Table 5. When considering the results together with those of Figure 5, however, the relative SiC/Si ratios point towards a more stoichiometric Si/C deposition when operating close to the central point of the design space.

Table 7: Relative phase amounts (weight %) of crystalline material for highest and lowest pressure and enthalpy runs.

	Low P	High P	Low H	High H
Si %	31.4	15.6	20.00	42.9
SiC %	68.6	67.2	33.3	52.0
Quartz %	-	-	16.5	-
Unidentified %	-	17.2	30.3	5.1
SiC/Si	2.18	4.31	1.67	1.21

All deposits are characterised by excess silicon, and initial consideration of the results indicates an increase in the amount of Si with an increase in enthalpy, accompanied by a decrease in Si with increasing pressure. This is in contrast to the expected occurrence of silicon-rich deposits at lower temperatures and higher pressures [33]. This is explained by considering that these values are only indicative of the crystalline material present in the deposits, and do not take into account the amount of amorphous material. It is therefore only evident that an increase in both pressure and enthalpy results in an increase in the amount of crystalline SiC and Si. Additionally, the preferred orientation of the deposits corresponds to the [111] and [220] crystal planes, giving much higher intensities relative to the [200] and [311] planes.
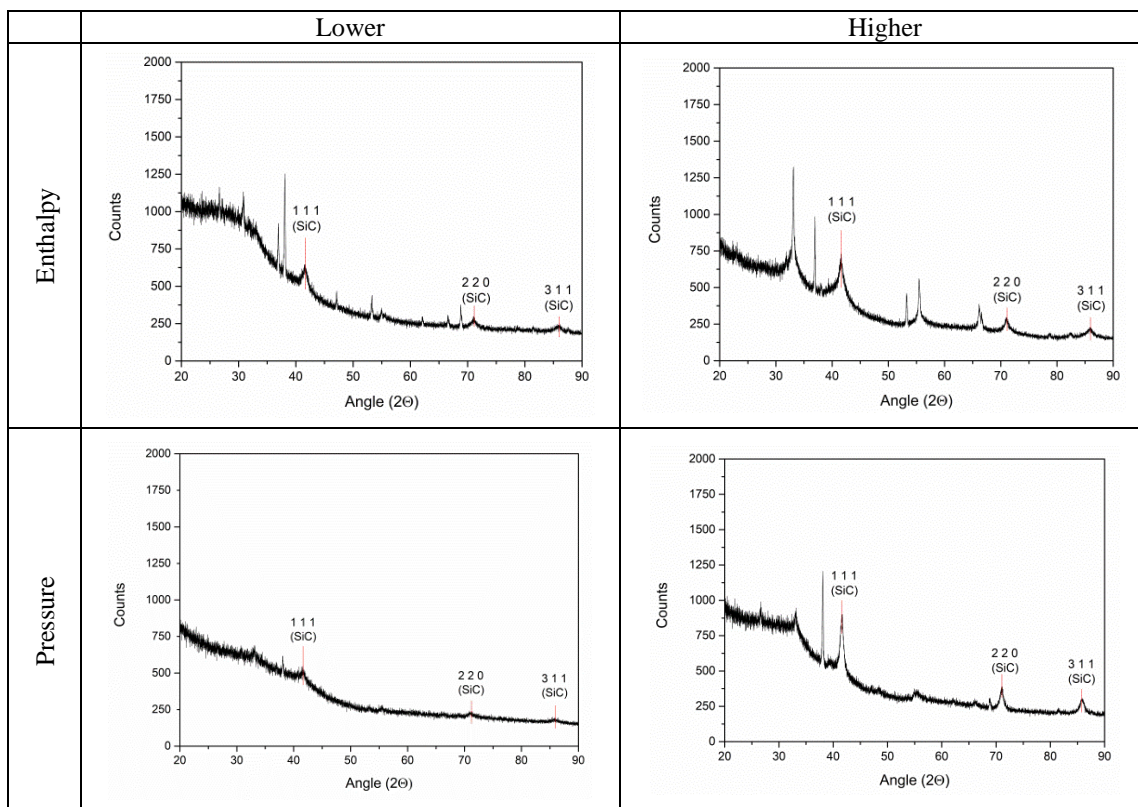
Figure 13: XRD spectra obtained from the minimum enthalpy (top left) and pressure (bottom left) as well as the maximum enthalpy (top right) and pressure (bottom right) runs, respectively.

3.4 Transmission Electron Microscopy

Particle sizes were probed using TEM characterisation. The collected powders were analysed for this purpose; an example is shown in Figure 14. The image showcases an agglomerated particle, consisting of nano-sized particles, with sizes below 100 nm.
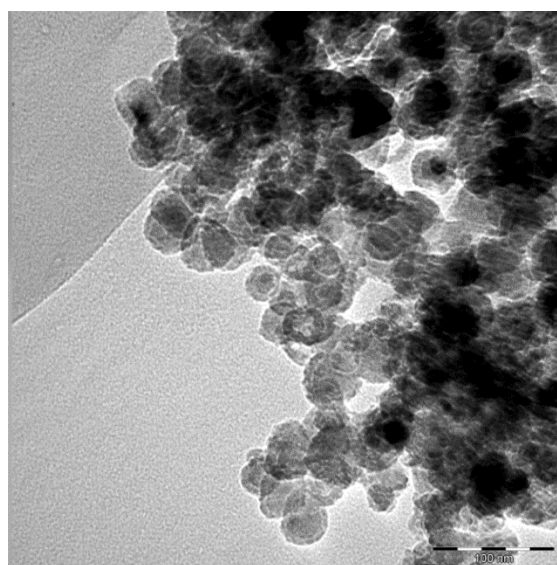

Figure 14: TEM image of nano-sized SiC particles.

3.5 Chemical Compound Analysis

The surface chemistry of the deposited layers was characterised using X-ray photoelectron spectroscopy (XPS), in order to semi-quantitatively identify chemical compounds present in the layer. The carbon (1s) and silicon (2p) orbital results were accordingly deconvoluted and are shown in Figure 15 for two experimental points, namely the central point (Exp #3) and Exp #10. These two points were chosen as they were vastly different in their optical colours, which could allude to a difference in chemical composition. The corresponding peaks and their possible chemical states were identified from the literature [34-36].

Electron Orbit	Exp #3	Exp #10
C 1s		
Si 2p		
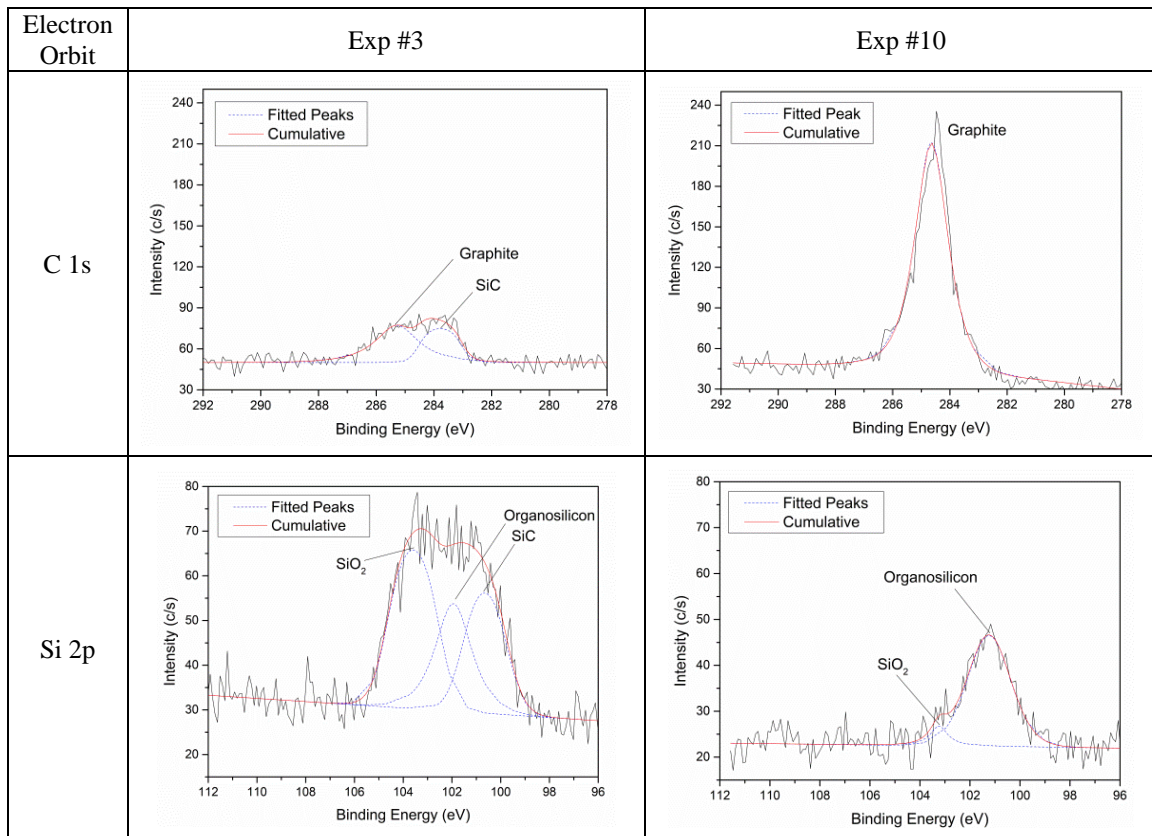
Figure 15: Comparison of XPS spectra for Exp #3 (left) and Exp #10 (right).

Exp #10 yielded a carbon-rich deposit, which might give rise to the darker colours seen in region VIII of Figure 9. This corresponds with low deposition pressures, where the silicon atoms desorb more rapidly [33]. The organosilicon peaks are likely indicative of unreacted or partially reacted MTS compounds embedded in the layers. In order to quantify the amount of organosilicon present in the layers, the corresponding powders from both of these runs were submitted for thermogravimetric analysis (TGA) in a nitrogen atmosphere; the results are shown in Figure 16.
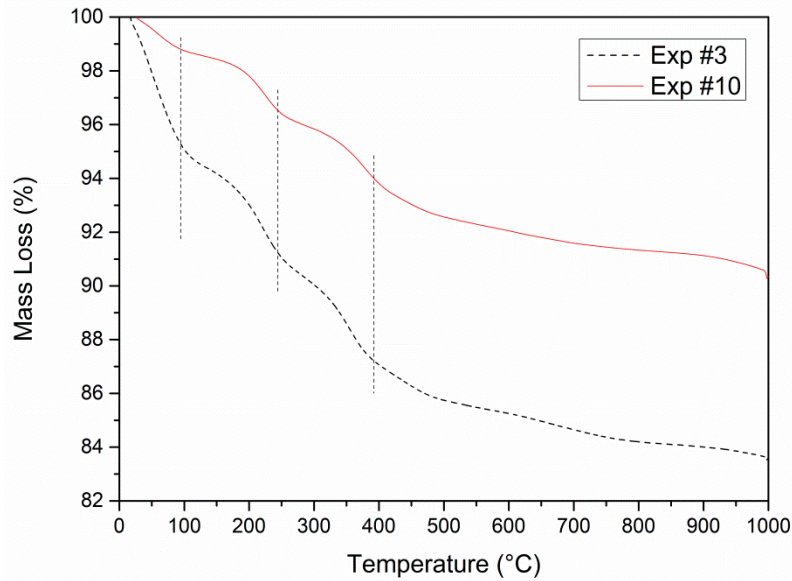
Figure 16: TGA results comparing the relative amounts of organosilicon between two samples.

Attempting to reduce the amount of organosilicon, the spheres from Exp #3 were annealed in air to 1000 °C, and characterised using XPS. The result for the Si (2p) orbital is shown in Figure 17 and compared to the same particle before annealing.
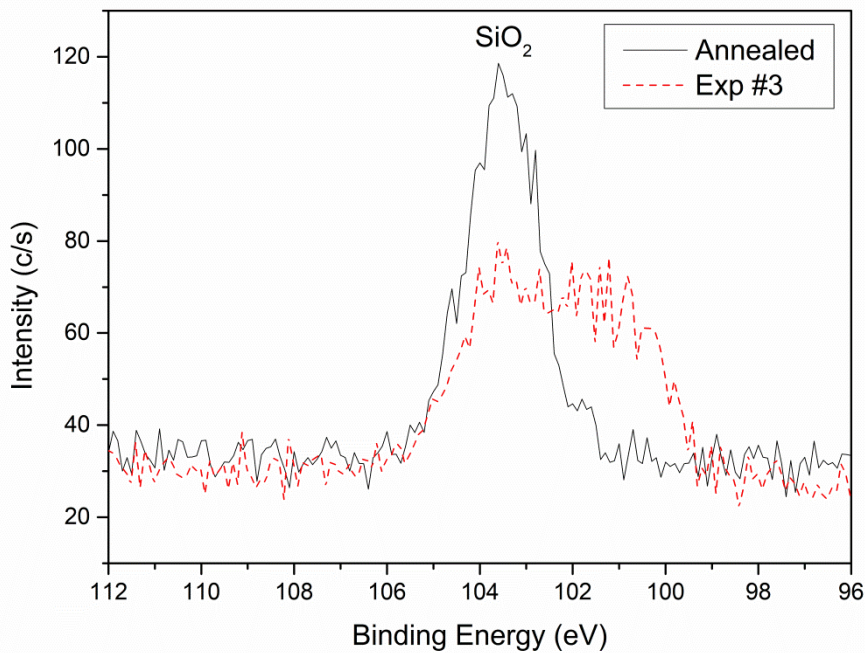

Figure 17: XPS comparison before and after annealing of the spheres.

The result is a marked decrease in both organosilicon and SiC, accompanied by a relative increase in silica (SiO_2) on the surface. Due to the annealing process having been undertaken in atmospheric conditions, the increase in SiO_2 is likely the result of an oxidation reaction of SiC on the surface of the layers.

The samples from the highest and lowest enthalpy and pressure experimental points were also submitted for XPS analysis. The results are given in Figure 18. Only the Si (2p) orbital spectra are shown here for conciseness.
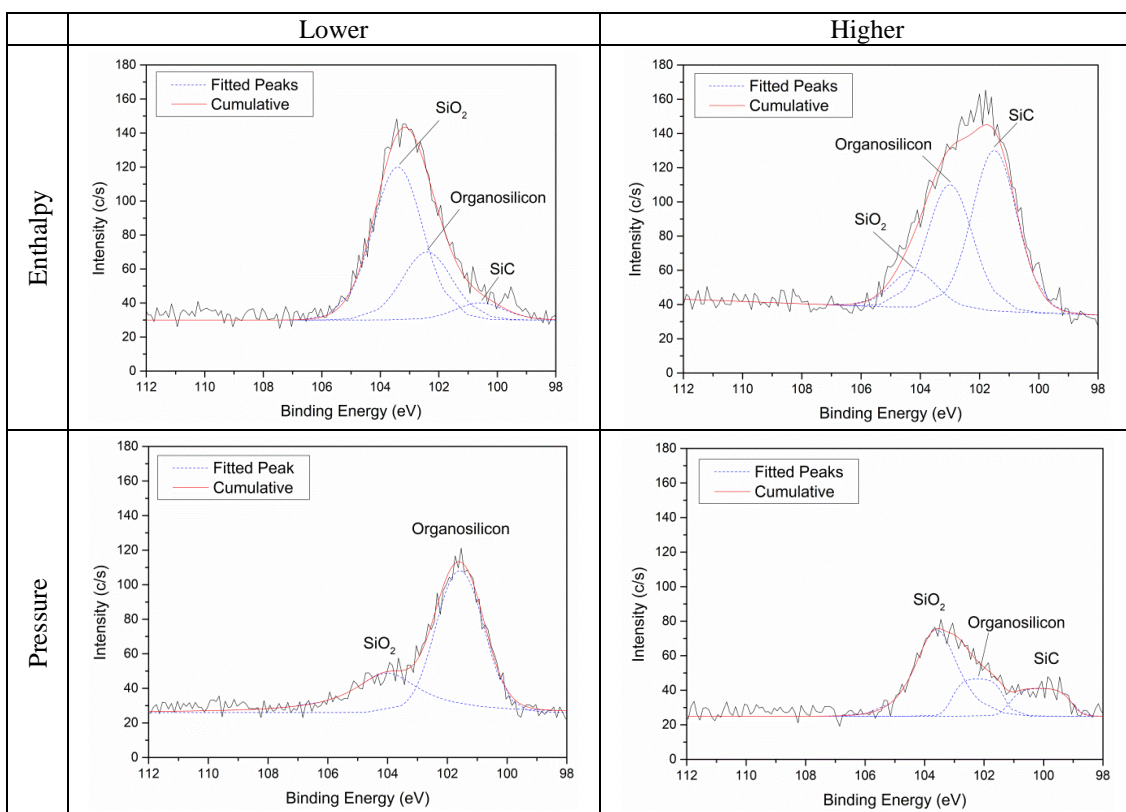
Figure 18: Si (2p) XPS results from the lower enthalpy (top left) and pressure (bottom left) and higher enthalpy (top right) and pressure (bottom right) experimental points.

As mentioned previously, XRD characterisation of the samples from the highest and lowest enthalpy and pressure experimental points (Figure 13) indicated that an increase in both enthalpy and pressure results in an increased amount of SiC. This trend is supported here with the XPS results from the same experimental points (Figure 18), which also demonstrates a relative increase in SiC with an increase in both enthalpy and pressure. The absence of silicon in the XPS results is likely due to the nature of the measurement technique, which limits the measurement area to the surface of the particles. It is expected that the free silicon on the surface has undergone oxidation and formed SiO_2, clearly evident in the XPS results. Likewise, SiO_2 is amorphous and does not appear on XRD measurements.

4. Conclusions

SiC layers were successfully deposited onto alumina particles in a microwave plasma-assisted spouted bed reactor. The design of experiment followed that of a 3-dimensional central composite design. Growth rates varied from 50 to 140 μm/h. The SiC layers were characterised using SEM, TEM, XRD, XPS, EDX and FTIR techniques, which assisted in developing a colour chart as well as a similar morphological chart used to indicate the change in morphology of the layers throughout the design space. High enthalpy and pressure values tended to produce darker coloured layers, often accompanied by carbon-rich deposits. XPS characterisation also indicated the presence of organosilicons, likely indicative of unreacted or partially reacted MTS compounds embedded in the layers. It is evident that within the design space, the optimal region for SiC deposition requires high enthalpy- (~5 MJ/kg) and pressure (>-60 kPa) conditions, with reasonable hydrogen-to-MTS ratios (~5:1). The quality (i.e. crystallinity, particle size, Si/C ratios) of the layers appears to improve at these conditions, at the expense of decreased deposition rates. Research towards optimal deposition parameters should include different substrate materials, varying plasma gasses, and mechanical testing of the layers (e.g. hardness tests).

5. Acknowledgements

6. References

1. Donald, I.W., B.L. Metcalfe, and R.N.J. Taylor, The immobilization of high level radioactive wastes using ceramics and glasses. Journal of Materials Science, 1997. 32(22): p. 5851-5887.
2. Katoh, Y., et al., Radiation effects in SiC for nuclear structural applications. Current Opinion in Solid State and Materials Science, 2012. 16(2012): p. 143-152.
3. High Temperature Gas Cooled Reactor Fuels and Materials, in IAEA TECDOC Series. 2010, INTERNATIONAL ATOMIC ENERGY AGENCY: Vienna.
4. Rohbeck, N. and P. Xiao, Evaluation of the mechanical performance of silicon carbide in TRISO fuel at high temperatures. Nuclear Engineering and Design, 2016. 306: p. 52-58.
5. Papasouliotis, G.D. and S.V. Sotirchos, Experimental study of atmospheric pressure chemical vapor deposition of silicon carbide from methyltrichlorosilane. Journal of Materials Research, 1999. 14(8): p. 3397-3409.
6. Wang, X., et al., Initial decomposition of methyltrichlorosilane in the chemical vapor deposition of silicon-carbide. Computational and Theoretical Chemistry, 2011. 967(2–3): p. 265-272.
7. Sone, H., T. Kaneko, and N. Miyakawa, In situ measurements and growth kinetics of silicon carbide chemical vapor deposition from methyltrichlorosilane. Journal of Crystal Growth, 2000. 219(3): p. 245-252.
8. Huran, J., et al., Amorphous silicon carbide thin films deposited by plasma enhanced chemical vapor deposition at different temperature for hard environment applications, in 21st International Symposium on Plasma Chemistry, A. von Keudell, et al., Editors. 2013: Queensland, Australia.
9. Sachdev, H. and P. Scheid, Formation of silicon carbide and silicon carbonitride by RF-plasma CVD. Diamond and Related Materials, 2001. 10(3–7): p. 1160-1164.
10. Honda, S., et al., SiC nanofibers grown by high power microwave plasma chemical vapor deposition. Applied Surface Science, 2003. 212–213: p. 378-382.
11. Lin, H., et al., Synthesis of amorphous silicon carbide nanoparticles in a low temperature low pressure plasma reactor. Nanotechnology, 2008. 19(32): p. 325601.
12. Tang, C., et al., Simultaneous formation of silicon carbide and diamond on Si substrates by microwave plasma assisted chemical vapor deposition. New Carbon Materials, 2008. 23(3): p. 250-258.
13. van Laar, J.H., et al., Microwave-plasma synthesis of nano-sized silicon carbide at atmospheric pressure. Ceramics International, 2015. 41(3, Part B): p. 4326-4333.
14. Vennekamp, M., et al., Formation of SiC nanoparticles in an atmospheric microwave plasma. Beilstein Journal of Nanotechnology, 2011. 2: p. 665-673.
15. Kaiser, M., K.M. Baumgärtner, and A. Mattheus, Microwave Plasma Sources -Applications in Industry. Contributions to Plasma Physics, 2012. 52(7): p. 629-635.
16. Karches, M., C. Bayer, and P. Rudolf von Rohr, A circulating fluidised bed for plasma-enhanced chemical vapor deposition on powders at low temperatures. Surface and Coatings Technology, 1999. 116–119: p. 879-885.
17. Shin, H.S. and D.G. Goodwin, Deposition of diamond coatings on particles in a microwave plasma-enhanced fluidized bed reactor. Materials Letters, 1994. 19(3): p. 119-122.

18. Sathiyamoorthy, D., Plasma spouted/fluidized bed for materials processing. Journal of Physics: Conference Series, 2010. 208(1): p. 012120.

19. Box, G.E.P., J.S. Hunter, and W.G. Hunter, Statistics for experimenters: design, innovation, and discovery. 2005: Wiley-Interscience.

20. Rusakov, G.V., et al., Peculiarities of preparing a-SiC:H films from methyltrichlorosilane. Applied Surface Science, 2001. 184(1): p. 128-134.

21. Fridman, A., Plasma Chemistry. 2008: Cambridge University Press.

22. Minato, K. and K. Fukuda, Chemical vapor deposition of silicon carbide for coated fuel particles. Journal of Nuclear Materials, 1987. 149(2): p. 233-246.

23. Zhang, W.G. and K.J. Hüttinger, CVD of SiC from Methyltrichlorosilane. Part II: Composition of the Gas Phase and the Deposit. Chemical Vapor Deposition, 2001. 7(4): p. 173-181.

24. Giesen, B., et al., Formation of Si-nanoparticles in a microwave reactor: Comparison between experiments and modelling. Journal of Nanoparticle Research, 2005. 7(1): p. 29-41.

25. Janzen, C., et al., Formation and in situ sizing of gamma-Fe2O3 nanoparticles in a microwave flow reactor. J Nanosci Nanotechnol, 2001. 1(2): p. 221-5.

26. Sugawara, H., et al., Behavior of microwave-heated silicon carbide particles at frequencies of 2.0–13.5 GHz. Applied Physics Letters, 2014. 105(3): p. 034103.

27. Isfort, P., et al., Silicon carbide as a heat-enhancing agent in microwave ablation: in vitro experiments. Cardiovasc Intervent Radiol, 2011. 34(4): p. 833-8.

28. Knipping, J., et al., Synthesis of high purity silicon nanoparticles in a low pressure microwave reactor. J Nanosci Nanotechnol, 2004. 4(8): p. 1039-44.

29. Szabó, D., Microwave Plasma Synthesis of Nanoparticles: From Theoretical Background and Experimental Realization to Nanoparticles with Special Properties, in Microwaves in Nanoparticle Synthesis. 2013, Wiley-VCH Verlag GmbH & Co. KGaA. p. 271-309.

30. Fu, L., et al., Microwave Plasma Synthesis of Nanostructured γ-Al2O3 Powders. Journal of the American Ceramic Society, 2003. 86(9): p. 1635-1637.

31. Bullot, J. and M.P. Schmidt, Physics of Amorphous Silicon–Carbon Alloys. physica status solidi (b), 1987. 143(2): p. 345-418.

32. Demichelis, F., C.F. Pirri, and E. Tresso, Influence of doping on the structural and optoelectronic properties of amorphous and microcrystalline silicon carbide. Journal of Applied Physics, 1992. 72(4): p. 1327-1333.

33. Chin, J., P.K. Gantzel, and R.G. Hudson, The structure of chemical vapor deposited silicon carbide. Thin Solid Films, 1977. 40: p. 57-72.

34. Moulder, J.F. and J. Chastain, Handbook of X-ray Photoelectron Spectroscopy: A Reference Book of Standard Spectra for Identification and Interpretation of XPS Data. 1995, Minnesota USA: Physical Electronics.

35. Johansson, L.I., F. Owman, and P. Mårtensson, High-resolution core-level study of 6H-SiC(0001). Physical Review B, 1996. 53(20): p. 13793-13802.

36. Arezzo, F., E. Severini, and N. Zacchetti, An XPS study of diamond films grown on differently pretreated silicon substrates. Surface and Interface Analysis, 1994. 22(1-12): p. 218-223.